Available online at www.sciencedirect.com
ScienceDirect
Journal of Power Sources 175 (2008) 98–105
JOURNAL OF POWER SOURCES
www.elsevier.com/locate/jpowsour

Combined measurement of PEMFC performance decay and water droplet distribution under low humidity and high CO

Toshiaki Murahashi *, Hiroyuki Kobayashi, Enju Nishiyama

Department of Electrical and Electronic Engineering, Fukui University of Technology, Gakuen 3-6-1, Fukui 910-8505, Japan

Received 11 April 2007; received in revised form 11 September 2007; accepted 13 September 2007
Available online 19 September 2007

Abstract

Measurements of the performance decay for a proton exchange membrane fuel cell (PEMFC) and the observation of water droplets were simultaneously carried out for 4000 h under degradation conditions of low humidity and high CO concentration. An optical cell was designed for observation of water droplets and measurement of the transition points.

It was found that as the performance decayed with time, the transition point to a two-phase flow moved toward the cathode exit for conditions of both low humidity and high CO concentration. Performance data showed that under these conditions, there was no pinhole in the membrane or significant mass transport loss observed. It was supposed that the deactivation of electrodes occurred at the cathode inlet and the anode outlet under low humidity and high CO concentration, and that this caused the decay in performance and observed change of the transition point at the cathode.

The change of the transition point was computed using a two-dimensional cell model. Performance decay, such as oxygen gain and the cell over-potential, was simulated by changing the value of the exchange current densities of the cathode and anode. Comparison with the experimental results shows good agreement for the total duration of cell operation.
© 2007 Elsevier B.V. All rights reserved.

Keywords: PEMFC; Degradation; Visualization; CO poisoning; Water droplet

1. Introduction

The proton exchange membrane fuel cell (PEMFC) has received much attention in the last decade as a promising candidate for a high-efficiency low-emission power source. However, there are still many hurdles that must be overcome to achieve operation of more than several ten thousands of hours for stationary applications. It is believed that durability and cost are the main hurdles for large-scale application [1]. With regard to durability, intensive studies have been carried out on membrane degradation, catalysts and catalyst support stability, impact of impurities, electrode degradation, fuel starvation and water management [2].

Water management is a key issue for the long-term operation of PEMFC. At low humidity, the proton exchange membrane and electrode assembly (MEA) loses water, which leads to a rapid increase of the ohmic resistance. On the other hand, if too much liquid water is present in the cell, the pores in the electrodes will be filled with water, obstructing the passage of reactant gases, a condition referred to as flooding. Visualization techniques have been shown to be powerful tools for investigating the formation and movement of water droplets and many studies have been reported [3–7].

In parallel, a modeling approach has been intensively investigated to explain the two-phase flow in a PEMFC [8–12]. However, there have been no reports on the study of performance decay under degradation conditions by the simultaneous observation of the change in distribution of water droplets. We assumed that under degradation conditions, the distribution of water vapor pressure, membrane resistance, and the current density in the plane of an electrode are changed with time, and that these changes should be reflected in the distribution of water droplets. Our previous study showed that a two-dimensional cell model was able to explain the transition point to a two-phase flow in the flow channels under the change of the gas utilization rate [13]. It is considered that this model can also be applied to

* Corresponding author. Tel.: +81 776 22 2549; fax: +81 776 29 7891.
E-mail address: murahasi@fukui-ut.ac.jp (T. Murahashi).

0378-7753/$ – see front matter © 2007 Elsevier B.V. All rights reserved.
doi:10.1016/j.jpowsour.2007.09.038

Nomenclature

a_j	activity of water in the stream j (a_a for anode, a_c for cathode)
C	concentration of water in the membrane (mol cm^{-3})
E_n	Nernst loss (V)
F	Faraday constant (96,485 C mol^{-1})
i_0	exchange current density (A cm^{-2})
I	local current density (A cm^{-2})
n_d	electro-osmotic drag coefficient
p	pressure (kPa)
R	gas constant (8.314 J mol^{-1} K^{-1})
t_d	dew point of the feed gas (°C)
t_s	cell temperature (°C)
T	temperature (K)
x	distance along the flow channel
y	coordinate perpendicular to the MEA
Z	magnitude of impedance (Ω)

Greek symbols

α	net drag of water per proton
δ	thickness (cm)
ξ	stoichiometry
η	over-potential (V)
θ	phase angle
σ	conductivity of membrane (1 Ω cm^{-1})

Subscripts

a	anode
c	cathode
con	condensation
in	inlet
m	membrane
out	exit

explain the change in the distribution of water droplets during performance degradation.

The purpose of this study is to investigate the decay of cell performance, which is accelerated by intentional degradation conditions, such as low humidity and high CO concentration. The performance decay can then be correlated with observations of the change in the water droplet distribution using an optical cell designed for visualization and a two-dimensional cell model.

2. Experimental

2.1. Optical cell for visualization

An optical cell was used to observe the distribution of liquid water droplets in the cathode [7,14]. The end plates of the cell were made from a transparent acrylic resin for the cathode and high-density carbon for the anode. A current collector, fabricated by the wire-cut method, was made from gold-plated stainless steel and a machined transparent flow field plate (cathode end plate), and these were engaged precisely with each other. The cell active area was 25 cm^2. The flow field was a single serpentine type and a counter-flow flow mode was used. The membrane electrode assembly (MEA) consisted of a membrane (Nafion 112), electrodes, and carbon-paper-type gas diffusion layers (GDL) were used. The catalyst loading level was 0.3 mg cm^{-2} for the anode and 0.5 mg cm^{-2} for the cathode. A water jacket, in which hot water was circulated in order to maintain an even temperature distribution, was set on the back of the anode end plate. Images of the water droplets on the back surface of the cathode GDL were recorded using a high precision digital camera.

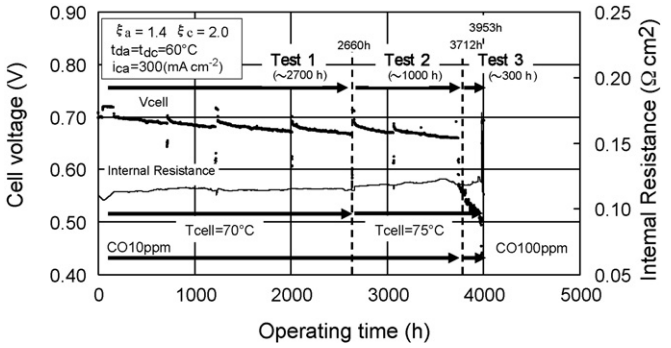

Fig. 1. Cell performance decay for 4000 h under conditions of low humidity and CO poisoning.

2.2. Performance measurement

The anode gas used was SRG(10) or SRG(100) or H_2, where SRG(10) represents a simulated reform gas (H_2/CO_2: 75/25 v/v) which contains 10 ppm CO. The feed gas was humidified by bubbling through a humidifier. The cathode gas used was air or oxygen. The cell temperature was maintained at 70 °C for the first 2700 h, and then raised to 75 °C for the remaining 1300 h (see Fig. 1).

The humidification temperature for both the anode and the cathode was 60 °C throughout the experiment. Measurements of oxygen gain, open circuit voltage (V_{oc}), internal resistance, and ac impedance were carried out at regular time intervals. The CO concentration was controlled at 10 ppm for the first 3700 h, and was then increased to 100 ppm for the remaining 300 h. The anode gas was changed from SRG(10) or SRG(100) to pure hydrogen, in order to confirm whether or not the activity of the anode catalyst was reversible. The experimental conditions for the present study are shown in Table 1.

Table 1
Operating parameters used for the base case

Current density, I (A cm^{-2})	0.3
Stoichiometry of anode gas, ξ_a	1.43
Stoichiometry of cathode gas, ξ_c	2.0
Humidity of cathode inlet gas, t_{dc} (°C)	60
Humidity of anode inlet gas, t_{da} (°C)	60
Cell temperature (°C)	70
Pressure (kPa)	101.3

2.3. ac impedance measurement

ac impedance measurements were conducted using an electric load (NF, AS5013, 0–50 A) and a frequency response analyzer (NF, FRA5095). A small ac current, equivalent to 5% of the load current applied to the cell, was superimposed over the frequency range of 10 kHz to 100 mHz under cell operation at 0.3 A cm^{-2}.

3. Experimental results

3.1. Performance decay with time under low humidification and high CO concentration

Cell performance was recorded for 4000 h under conditions of low humidity and CO poisoning; the results are shown in Fig. 1. The cell voltage gradually decreased with time, although it recovered when SRG was replaced with pure hydrogen. The initial cell voltage was 704 mV at a current density of 300 mA cm^{-2} and the performance decay rate was 10 mV 1000 h^{-1} for operation with SRG(10). After 3700 h of operation, the CO content was increased to 100 ppm. A significant loss of performance was observed, from 657 mV to 485 mV (shown in Fig. 1) in 300 h of operation. The internal resistance increased continuously with time.

Fig. 2 shows the time dependence of the open circuit voltage (V_{oc}) and oxygen gain. At the beginning of the test the V_{oc} value is 967 mV, and 939 mV after 3953 h of operation. From the observed 28 mV drop in the V_{oc}, it is unlikely that any damage occurred to the electrolyte membrane, such as pinhole formation, within the time span of 3953 h.

The oxygen gain was moderately increased from 82 mV to 85 mV over the first 2000 h (1.5 mV 1000 h^{-1}). Oxygen gain usually reflects the diffusion loss mostly by the flodding in the cathode catalyst layer and GDL. The flooding causes the local increase of the current density in the forward section which

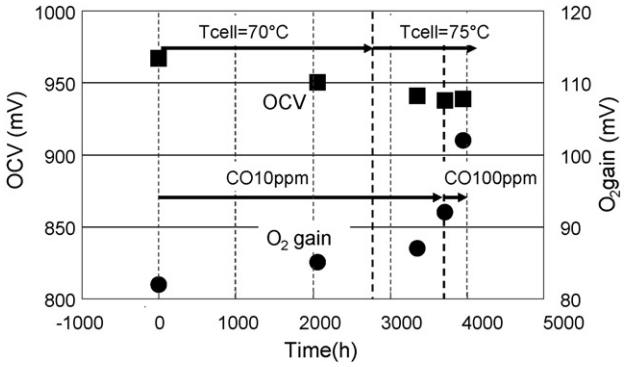

Fig. 2. Time dependence of the open circuit voltage (OCV) and oxygen gain: (■) OCV; (●) oxygen gain.

is contrary to the change of the transition position shown in Fig. 5. This means that the mass transport loss was negligibly small during this period of time. However, after the temperature increase to 75 °C, the oxygen gain increased rapidly by a rate of 4 mV 1000 h^{-1} The experimental results described here are summarized in Table 3.

It is considered that the increase in the oxygen gain reflects the deactivation of the cathode catalyst layer by the loss of triple boundary interfaces, due to the low-humidity condition. This causes a local increase of current density at the cathode exit area. Increase of the CO concentration caused a large increase of oxygen gain up to 102 mV. The increase in the oxygen gain reflects the deactivation of the anode catalyst due to the CO poisoning, and the local and concentrated increase of current density in the cathode.

3.2. Electrochemical impedance spectroscopy (EIS) with time

EIS data were measured when the experimental conditions were changed during cell operation. Fig. 3 shows the relation

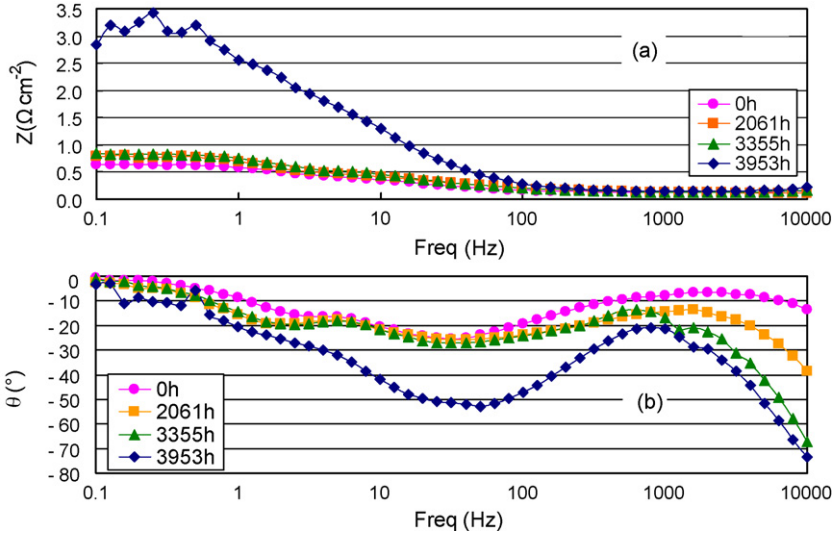

Fig. 3. Change in the impedance magnitude and phase angle vs. frequency: (a) impedance magnitude (Z) vs. frequency and (b) phase angle (θ) vs. frequency. (●) start; (■) 2061 h; (▲) 3355 h; (♦) 3953 h.

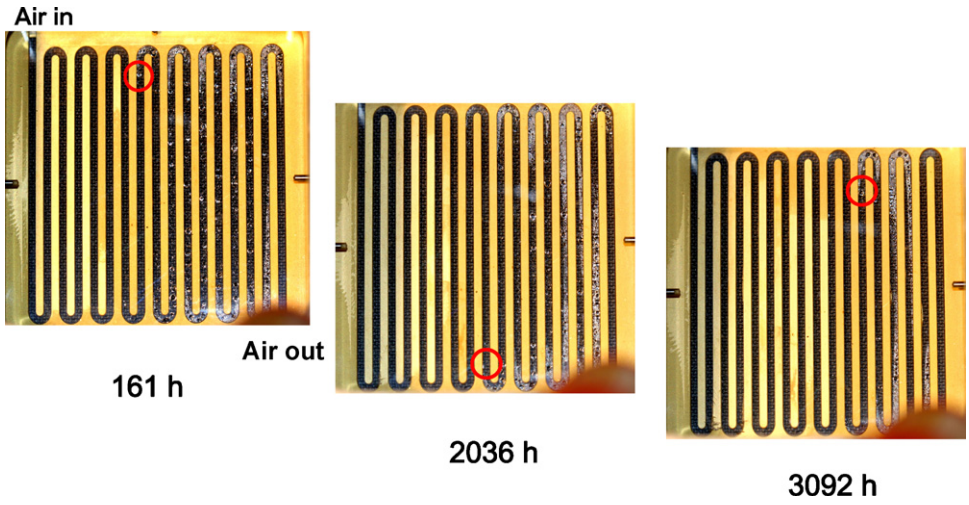

Fig. 4. Photographs of the visualized images of water droplets at 161 h, 2036 h and at 3092 h: (◯) the location where a water droplet is first observed in the flow channel.

of frequency versus magnitude of impedance, Z (Fig. 3(a)) and phase angle, θ (Fig. 3(b)). For the first 3700 h (CO, 10 ppm), the impedance increased slightly in the range of less than 100 Hz, but when the CO concentration was increased from 10 ppm to 100 ppm, the impedance magnitude was almost five times larger after 300 h of operation with high CO concentration (100 ppm).

Canut et al. [15] performed EIS investigations of anode catalyst poisoning, fuel cell flooding and membrane drying. They showed that anode catalyst poisoning due to CO is characterized by an increase in the impedance magnitude and the phase angle at frequencies less than a few hundred Hz. Our result, shown in Fig. 3, also shows this characteristic increase in the impedance magnitude and the phase angle.

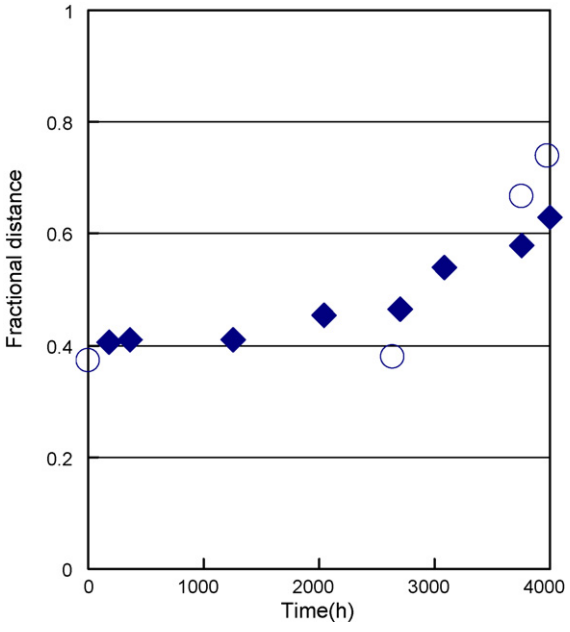

Fig. 5. Change of the transition points in the cathode with time duration: $T_{cell} = 70\,^{\circ}C$ and $75\,^{\circ}C$, $0.3\,A\,cm^{-2}$, $t_{da} = t_{dc} = 60\,^{\circ}C$, $\xi_a = 1.4$, $\xi_c = 2.0$. (♦) Experiment; (◯) calculation.

3.3. Change in the distribution of water droplets in the cathode gas diffusion layer over time

Fig. 4 shows photographs of the visualized images of water droplets at 161 h, 2036 h and at 3092 h The circles in each photo indicate the location where a water droplet is first observed in the flow channel. This point is the location where the water vapor pressure reaches the saturation vapor pressure at the cell temperature. At the beginning (161 h), water droplets were distributed in the latter half of the electrode area, and the transition point to the two-phase flow was located at 0.4 of the fractional distance from the inlet to the exit. No water droplets were found in the area near the inlet. It can be clearly seen in Fig. 5 (♦), that the transition point moves toward the exit over time, and that the slope becomes steeper when the cell temperature is increased to 75 °C.

4. Discussion

4.1. Cell model for simulation

As described in Section 3, the experimental results showed that the distribution of water droplets changes with the degradation in cell performance over 4000 h of operation under low humidity and high CO concentration. To understand the observed change, a two-dimensional cell model [14] is applied, which can account for the water content in the membrane, the mass transport of water and the current density distribution along the flow channel.

In both the cathode and the anode, gas diffusion in the y-direction (perpendicular to the MEA) is expressed by the Stefan–Maxwell equations, using the effective binary diffusivities. Both nitrogen in the cathode gas mixture and carbon dioxide in anode gas mixture do not react in their respective electrode reactions. The change of current density along the flow channel, $I(x)$, is calculated using Eqs. (1)–(5) concerning the membrane ion conductivity and over-potential, and the Nernst loss under the condition of uniform cell voltage along the

flow channel. Both cathode and anode overpotentials are given by the Butler–Volmer equation (B–V eq.). We have chosen the value $n\alpha = 2/3$ for the cathode reaction, by fitting the calculated overpotential with the experimental results. The cathode overpotential shown by Eq. (3a) is derived from a simplification of the B–V eq. under the condition where η_c is large. The anode over-potential, shown by Eq. (3b), is also derived from a simplification of the B–V eq. under the condition where η_a is small. The Nernst loss, E_n, is derived by replacing the activities of hydrogen and oxygen gases by their partial pressures. The open circuit voltage, V_{oc}, decreases from the thermodynamic value due to the leakage current, j_{leak}, which is estimated at 0.01 A cm^{-2} [16].

$$V = V_{oc} - \frac{I(x)\delta_m}{\sigma} - (\eta_c + \eta_a) - E_n \quad (1)$$

$$\sigma = (0.00514 \times 8.8 n_d - 0.00326) \times \exp\left(1267\left(\frac{1}{303} - \frac{1}{T}\right)\right) \quad [9] \quad (2)$$

$$\eta_c = \frac{1.5RT}{F} \ln\left(\frac{I(x)}{i_{0_c} p_{O_2}}\right) \quad (3a)$$

$$\eta_a = \frac{1}{2}\frac{RTI(x)}{Fi_{0a} p_{H_2}} \quad (3b)$$

$$E_n = \frac{RT}{2F} \ln\left(\frac{1}{p_{H_2}\sqrt{p_{O_2}}}\right) \quad (4)$$

$$V_{oc} = 1.229 - 0.00023\,(T - 298) - \frac{1.5RT}{F} \ln(j_{leak}) \quad (5)$$

where [9]

$$n_d = \begin{cases} 0.049 + 2.024 a_a - 4.53 a_a^2 + 4.09 a_a^3 & a_a \le 1 \\ 1.59 + 0.159\,(a_a - 1) & a_a \ge 1 \end{cases}$$

$$a_j = C_j \frac{p}{p_{sat}}$$

In the model, the cell is divided into five sections in the x-direction (flow direction). In each section, the mass balances of each gas species are expressed as a set of non-linear equations for counter-flow configurations. These sets of equations are solved by the Newton method. Hence, the distribution of current density, net water drag and contents of gas species are obtained along the flow channel. The parameters of the MEA and GDL used for the calculation of the base case are listed in Table 2.

Table 2
Parameters used for the MEA component

Exchange current density, i_{0c} (A cm^{-2})	0.01
Exchange current density, i_{0a} (A cm^{-2})	1
Membrane equivalent weight, E	1200
Membrane thickness, δ_m (cm)	50×10^{-4}
Membrane dry density, ρ	1.84
Catalyst layer thickness, δ_{cat} (cm)	10×10^{-4}
GDL thickness (cm)	300×10^{-4}
Tortousity factor	5.0
Diffusion coefficient, D_{eff,H_2O,O_2} (cm^2 s^{-1})	0.0043
Diffusion coefficient, D_{eff,O_2,N_2} (cm^2 s^{-1})	0.0033

4.2. Transition point to two-phase flow

4.2.1. Exchange current density and transition point

Irreversible damage to the membrane, such as formation of pinholes, did not occur (as seen from the V_{oc} results), and the mass transport losses were small (from the oxygen gain results), so that it was supposed that the decay of cell performance was mainly caused by the deactivation of the electrodes, which corresponds to the change in the exchange current densities used in Eqs. (3a) and (3b). Computation of the transition point was conducted by changing the value of the exchange current density at section 1 of the cell (the section nearest to the cathode inlet and the anode exit). At section 1, dehydration is significant in the cathode, resistance of the ionomer in the catalyst layer is high, and utilization of the catalyst is low. Also under the high CO concentration, it is supposed that the deactivation of anode catalyst has occured in all cell area and its rate is significant in section 1. These factors cause the deactivation of the cathode catalyst in the inlet area and the anode catalyst in the anode exit area. Under the standard experimental conditions (Table 1), the exchange current densities of the cathode and anode ($i_{0c} = 0.01$ A cm^{-2} [9] and $i_{0a} = 1$ A cm^{-2} [16]) are assumed to be uniform over the entire cell area. However, the exchange current density is not uniform over the cell area when local deactivation of the electrode occurs. For example, degradation of the cathode catalyst at the cathode inlet, and of the anode catalyst at the anode exit, is expected to be significant under conditions of dry operation in the cathode and high CO concentration in the anode gas.

These effects were reflected in the cell model. The computed results of transition point versus exchange current density under the standard condition are shown in Fig. 6(a) and (b). Fractional distance of the transition point was calculated using the following equation under the condition that the build up of the water content in each section is uniform.

$$\int_0^{x_{con}} \frac{I(x)}{2F}(1 + 2\alpha(x))\,dx = m_{H_2O,sat}(x) - m_{H_2O,in}$$

where X_{con} is the distance from cathode inlet to transition point, $I(x)$, $\alpha(x)$ represents current density and net drag coefficient as the function of distance (x) from the inlet, respectively. m_{H_2O} represents molar flux of water and the saturation molar flux $m_{H_2O,sat}(x)$ is calculated using the local partial pressure of water vapor.

The results show that the transition point shifts towards the exit, from 0.49 to 0.61, when the cathode exchange current density at the cathode inlet is decreased to one tenth. In addition, the transition point shifts towards the exit from 0.49 to 0.63 as the anode exchange current density at the anode outlet decreases from 1 A cm^{-2} to 0.005 A cm^{-2}.

During cell operation, the temperature of the cathode transparent plate was approximately 2–3 °C lower than the cell temperature. Therefore, saturation temperatures for the cathode flow channel of 68 °C and 72 °C were employed in the calculation against cell temperatures of 70 °C and 75 °C, respectively.

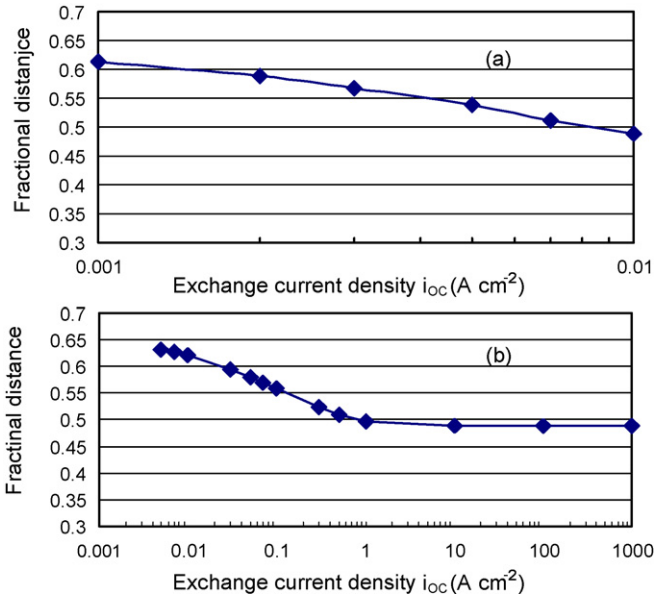

Fig. 6. (a) Computed results of transition point vs. cathode exchange current density, i_{0c}, under the standard conditions ($T_{cell} = 70\,^{\circ}C$, $t_{dc} = t_{da} = 60\,^{\circ}C$). The varied parameters in (a) are i_{oc} in section 1 only. (b) Computed results of transition point vs. anode exchange current density, i_{0a}, under the standard conditions ($T_{cell} = 70\,^{\circ}C$, $t_{dc} = t_{da} = 60\,^{\circ}C$). The varied parameters in (b) are i_{0a} in section 1 only.

4.2.2. Change in the exchange current density with low humidity and CO poisoning

Under low humidification, it is supposed that dehydration of the membrane and the ionomer in the catalyst layers cause a voltage drop [17]. We assume that the degradation of the cathode only occurs in section 1, because the humidity of the cathode gas reaches to almost saturated between sections 2 and 5. The degradation of the anode occurs in all cell area but the degree of the degradation depends on cell location. We suppose the degradation in section 1 is 10 times higher than the remaining sections.

Computation of the performance decay was conducted under conditions where the cathode exchange current density, i_{0c}, at the cathode inlet varies from 0.01 A cm^{-2} to 0.009 A cm^{-2} for the first 2700 h (70 °C operation, Test 1) and then varies from 0.009 to 0.008 A cm^{-2} for the next 1000 h (75 °C operation, Test 2), while the anode exchange current density, i_{0a}, is maintained at the initial value. This is rationalized by the fact that the EIS data (Fig. 3) shows a very small change in the impedance magnitude over time until 3700 h (10 ppm CO), which means the degree of deactivation at the anode due to CO poisoning is very small, as Canut et al. suggested in their report [15].

After 3700 h (Test 3), the i_{0a} at the anode exit varied from 1 A cm^{-2} to 0.005 A cm^{-2}, reflecting severe CO poisoning (100 ppm CO), which corresponds to a large increase in the magnitude of impedance in the range of 1–100 Hz, as shown in Fig. 3. The anode exchange current density of the remaining area is 0.05 A cm^{-2}. A comparison of the calculated and the experimental results is given in Fig. 5. Although the computed points are slightly closer to the cathode inlet for the first 2700 h, and are slightly closer to the cathode outlet for the final 300 h, the computed results are in good agreement with the experimental results.

4.3. O_2 gain and cell over-potential

The experimental and computed values for oxygen gain and the cell over-potential, represented by the value ($V_{oc} - V$, namely, $\eta_c + \eta_a + (I\delta_m/\sigma) + E_n$) at several key points, are listed in Table 3. The computed values are compared with the experimental results and are presented in Fig. 7(a) and (b). Fig. 7(a) shows the comparison of the absolute values of oxygen gain and over-potential, and Fig. 7(b) shows the comparison of the change in oxygen gain and cell over-potential measured as the difference from the starting values. Although the computed oxygen gain is approximately 10–20 mV higher than the experimental value, the increment from the starting value of the oxygen

Table 3
List of the parameters used in the calculation and the results of experiment and computation

	Time							
	0 h	2061 h	2660 h	3355 h	3712 h	3953 h	3712 h	3953 h
t_s	70	70	70	75	75	75		
i_{0c} 1	0.01		0.009	0.009	0.008	0.008		
i_{0c} 2–5	0.01		0.01	0.01	0.01	0.01		
i_{0a} 1	1		1		1	0.005		
i_{0a} 2–5	1		1		1	0.05		
$V_{cell,air}$, calc	713		712		685	582		
$V_{cell,o2}$, calc	817		815		802	702		
V_{oc}, calc	1014		1014		1010	1010		
$V_{cell,air}$, exp	704	679		665	657	518		
$V_{oc,air}$, exp	967	950		941	938	939		
O_{2gain}, exp	82	85		87	92	102	10	20
O_{2gain}, calc	104		104		117	120	13	16
Total loss, exp	263	271		276	281	421	18	158
Total loss, calc	301		302		325	428	24	127

The last two columns represent the differences of the value of each item from the initial (0 h) values.

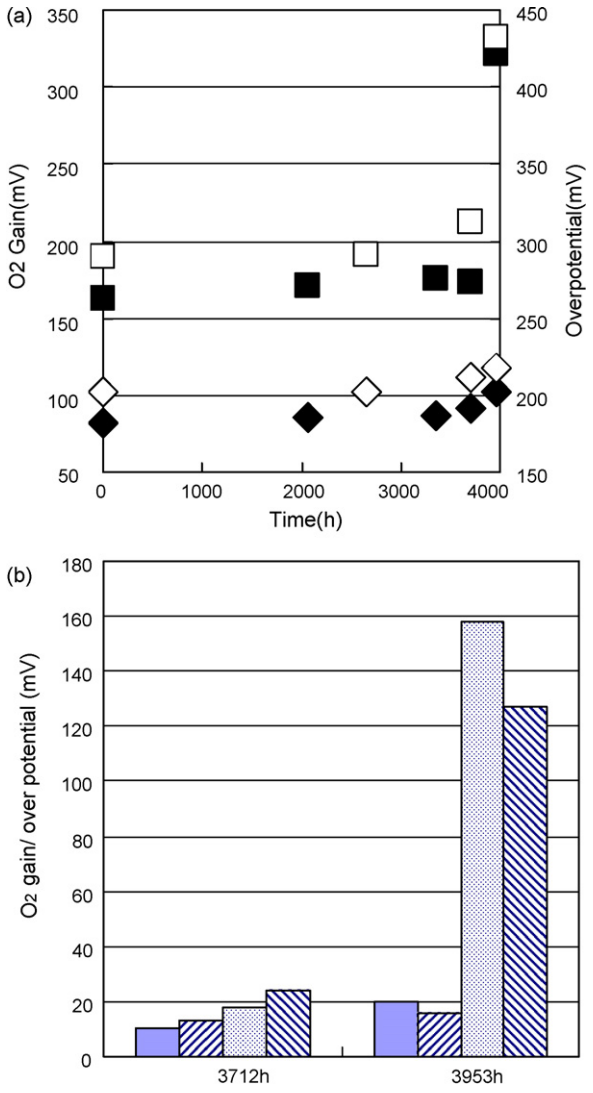

Fig. 7. (a) Comparison of the cell performance and oxygen gain with the computed results: $T_{cell} = 70$, 75, 0.3 A cm^{-2}, $\xi_a = 1.4$, $\xi_c = 2.0$. (□) total loss/calculation; (■) total loss/experiment; (◇) oxygen gain/calculation; (◆) oxygen gain/experiment. (b) Comparison of the change in oxygen gain and cell over-potential measured as the difference from the starting values. Each bar is from left, oxygen gain/experiment, oxygen gain/calculation, total loss/experiment, total loss/calculation, respectively.

gain shows good agreement. After 1000 h of operation at 75 °C (total 3712 h, the end of Test 2), a 13 mV increase of oxygen gain is computed, in comparison to the 10 mV increase observed for the experiment. After 300 h of operation using SRG containing 100 ppm CO (total 3953 h, the end of Test 3), the computation showed a 16 mV increase in the oxygen gain, compared to the 20 mV increase observed for the experiment.

With respect to the cell over-potential, the computed results explain the experimental trend well, showing a steady increase for the first 3700 h, and subsequently, a rapid increase at high CO concentration. The calculated result for the over-potential, including resistance loss, is 127 mV, which is slightly low compared to that (158 mV) obtained from the experiment (Table 3 and Fig. 7(b)).

5. Conclusion

Measurements of performance decay for a PEMFC under degradation conditions, and the observation of water droplets were carried out simultaneously for a long period of operation (4000 h). The degradation conditions were low humidity and high CO concentration. Water droplets were observed using an optical cell designed for visualization.

It was found that as performance decay progressed with time, the transition point to a two-phase flow moved toward the cathode exit for both conditions of low humidity and high CO concentration. The performance data under these conditions show that no membrane pinholes or significant mass transport losses occurred. We consider that the decay in cell performance was caused by the deactivation of the cathode and anode, which corresponds to the change in the exchange current densities. The transition point was calculated by the change in the value of the exchange current densities at section 1 of the cell (cathode outlet and anode inlet).

Comparison of the experimental transition point to the two-phase flow shows good agreement for the entire duration. Performance decay, such as oxygen gain and the total cell voltage loss ($V_{oc} - V$) were also calculated and the results simulate the experimentally observed trend well.

Simultaneous measurements of performance decay and water droplets on the cathode enabled visual observation of the degradation of electrode activity and confirmation using simulated data.

Acknowledgements

This work was supported by Research and Development of Polymer Electrolyte Fuel Cells from the New Energy and Industrial Technology Development Organization (NEDO), Japan, and by the Open Research Center Project from the Ministry of Education, Culture, Sports, Science and Technology, Japan.

References

[1] H. Gasteiger, W. Gu, R. Makharia, M. Mathias, B. Sompalli, in: W. Vielstich, A. Lamm, H. Gasteiger (Eds.), Handbook of Fuel Cells, vol. 3, John Wiley & Sons, New York, 2003, pp. 593–677.
[2] T. Jarvi, S. Cleghorn, H. Gasteiger, ECS Trans. 1 (8) (2006).
[3] T. Tüber, D. Pocza, C. Hebling, J. Power Sources 124 (2003) 403–414.
[4] X.G. Yang, F.Y. Zhang, A.L. Lubawy, C.Y. Wang, Electrochem. Solid State Lett. 7 (2004) A408–A411.
[5] J. Zhang, D. Kramer, R. Shimoi, Y. Ono, E. Lehmann, A. Wokaun, K. Shinohara, G.G. Scherer, Electrochim. Acta 51 (2006) 2715–2727.
[6] F.Z. Zhang, X.G. Yang, C.Y. Wang, J. Electrochem. Soc. 153 (2006) A225–A232.
[7] T. Murahashi, H. Kobayashi, E. Nishiyama, Electrochemistry 76 (2007) 261–263.
[8] T.E. Springer, T.A. Zawodzinski, M.S. Wilson, S. Gottesfeld, J. Electrochem. Soc. 143 (1996) 587–599.
[9] T.V. Nguyen, R.E. White, J. Electrochem. Soc. 140 (1993) 2178–2186.
[10] G.J.M. Janssen, J. Electrochem. Soc. 148 (2001) A1313–A1323.
[11] A. Weber, J. Newman, J. Electrochem. Soc. 151 (2004) A326–A339.
[12] C.Y. Wang, Chem. Rev. 104 (2004) 4727–4766.
[13] T. Murahashi, M. Naiki, E. Nishiyama, J. Power Sources 162 (2006) 1130–1136.

[14] T. Murahashi, H. Hayashi, E. Nishiyama, The 11th FCDIC Fuel Cell Symposium Proceedings, FCDIC, Tokyo, 2004, pp. 111–116.
[15] J. Canut, R. Abouatallah, D. Harrington, J. Electrochem. Soc. 153 (2006) A857–A864.
[16] R. O'Hayre, S. Cha, W. Colella, F. Printz, Fuel Cell Fundamentals, John Wiley & Sons, 2006, p. 172.
[17] M. Inaba, H. Yamada, R. Umebayashi, M. Sugishita, A. Tasaka, Electrochemistry 76 (2007) 207–212.